Time-domain surface plasmon polaritons on a graphene sheet

Paolo Burghignoli*
Department of Information Engineering, Electronics and Telecommunications, Sapienza University of Rome, via Eudossiana, 18-00184 Rome, Italy

Giampiero Lovat, Rodolfo Araneo, and Salvatore Celozzi
Electrical Engineering Division of DIAEE, Sapienza University of Rome, via Eudossiana, 18-00184 Rome, Italy

(Received 12 February 2018; revised manuscript received 6 June 2018; published 20 June 2018)

A time-domain analysis is presented of the transient field excited by a vertical electric dipole on a graphene sheet described through a local scalar conductivity model valid in the intraband regime. The analysis is carried out by means of the double-deformation method of Tsang and Kong [J. Math. Phys. **20**, 1170 (1979)], a modified modal technique which allows for defining a causal surface-plasmon-polariton (SPP) contribution to the total transient field that is also computationally very efficient for a graphene sheet. Numerical results are presented and validated against independent numerical full-wave simulations. The proposed approach provides a viable route to the direct time-domain investigation of the role of SPPs in graphene-based structures employed in ultra-wide-band nanosystems.

DOI: 10.1103/PhysRevB.97.245418

I. INTRODUCTION

The excitation of surface plasmon polaritons (SPPs) on graphene sheets and nanoribbons has been the subject of intense research in the last decade [1–4], thanks to the opportunities offered by their high-field confinement, long propagation distance, and especially by the possibility of controlling their propagation properties in real time via an ambipolar electric-field effect through the simple application of an external voltage [5–7]. SPPs belong to the modal spectrum of graphene nanowaveguides and therefore their electromagnetic characterization is customarily performed via time-harmonic dispersion analyses in the frequency domain (FD), based on both local and nonlocal models for the graphene conductivity [8–13]. As concerns their excitation by means of finite sources, the vast majority of the existing literature is also focused on the time-harmonic regime [14–18]. A direct time-domain (TD) analysis of the transient excitation of graphene sheets is however necessary for studying nonlinear effects [19] and would also be more convenient in the linear regime for ultra-wide-band applications, where ultrashort pulses are typically used as input wave forms [20]. In fact, besides considerable computational advantages, a TD analysis would afford valuable physical insights into the relevant transient wave phenomena which, as is well known, are distinct from those typical of the time-harmonic regime [21].

In this framework, a TD analysis of the transverse-electric (TE) field excited by an electric line source parallel to a graphene sheet was carried out using a modified Cagniard–de Hoop (CdH) technique [22], assuming a local graphene conductivity dominated by the relevant intraband contribution [8]. In this regime, however, the SPP supported by the sheet is transverse magnetic (TM) [10], and therefore it is not excited by the considered source. This analysis has been recently extended to the case of a vertical electric-dipole (VED) source, which produces an azimuthally symmetric TM field and is thus capable of exciting an omnidirectional cylindrical SPP wave along an infinite graphene sheet [23]. However, the CdH method is an intrinsically *nonmodal* technique, which allows for conveniently calculating the total field but is not capable of sorting out the relevant SPP contribution.

In this paper we address the problem of performing a TD *modal* analysis of the field excited by a VED on a graphene sheet described through a local impedance boundary condition in the intraband regime (see Fig. 1) in order to achieve a direct characterization of the transient SPP wave form. Such a characterization is, to the best of our knowledge, still missing in the literature and aims at addressing the longstanding problem of properly defining the SPP in the TD from exact solutions of the time-dependent Maxwell equations. To this aim, we employ the double-deformation technique (DDT) first proposed by Tsang and Kong [24].

Focusing on the magnetic induction excited on the graphene sheet, its standard expression as a double inverse-Fourier/inverse-Hankel transform is manipulated in two steps, by performing in sequence two deformations of the relevant complex integration paths, first in the radial-wave-number plane and then in the radian-frequency plane, to suitable steepest-descent paths (SDPs). The total induction is thereby represented as a sum of residue contributions arising from the poles captured in the deformation process plus a double-integral SDP contribution.

Note that the standard SPP field is well defined in the FD as the residue contribution of the relevant pole in the radial-wave-number plane. Furthermore, it is known to provide the dominant contribution to the field excited by a nanoemitter located in proximity of the graphene sheet, in a radial range

*burghignoli@diet.uniroma1.it

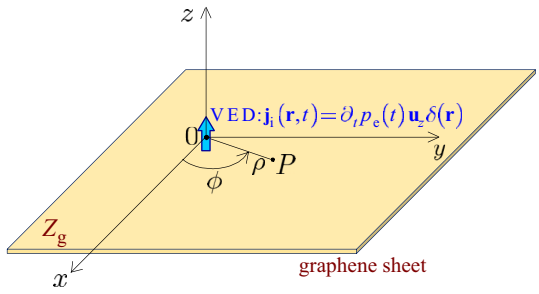

FIG. 1. An infinite graphene sheet placed in vacuum on the $z = 0$ plane, excited by a transient vertical electric dipole (VED) with electric-dipole moment $p_e(t)\mathbf{u}_z$ placed at the origin of the Cartesian reference system. The graphene sheet is described in the frequency domain through a local, scalar surface impedance $Z_g = R_g + j\omega L_g$. Polar coordinates (ρ,ϕ) are also shown for an observation point P located on the sheet.

up to tens or even hundreds of wavelengths from the source [15]. On the other hand, its direct TD counterpart obtained via a temporal inverse Fourier transform does not provide a physically valid TD SPP. In fact, the analysis presented here shows that the field resulting from such a direct inversion would be noncausal and possibly also nondominant, depending on the observation point and time. In contrast, the DDT allows for pairing it with a second contribution, arising from a suitable SPP-related pole singularity in the radian-frequency plane, which is able to restore both causality and dominance to the resulting field, which can then be properly defined as a TD SPP field.

In addition to providing a viable route to TD SPPs, the DDT-based approach is also computationally very efficient for thin planar structures because of the reduced number of involved poles [25,26], even more so for a graphene sheet that, as said, supports a *single* TM SPP and for which it will be shown that all the involved poles are known in analytical form.

II. STRUCTURE DESCRIPTION AND BACKGROUND

A. The configuration under analysis

We consider here an infinite graphene sheet placed on the plane $z = 0$ in a vacuum with permittivity ε_0, permeability μ_0, and light velocity $c_0 = 1/s_0 = 1/\sqrt{\varepsilon_0\mu_0}$ (see Fig. 1). The sheet is excited by a short, vertically directed electric-current source with density $\mathbf{j}_i(\mathbf{r},t)$ [A/m^2], characterized by a length ℓ [m] and total current $i(t)$ [A].

By retaining the lowest-order (electric-dipole) term in a multipole expansion of the source, this can be collapsed to a point VED, which can be assumed without loss of generality to be located on the z axis, i.e., $\mathbf{j}_i(\mathbf{r},t) = i(t)\ell\delta(x)\delta(y)\delta(z - z_0)\mathbf{u}_z$, where $\delta(\cdot)$ indicates the Dirac δ distribution. Note that $i(t)\ell\mathbf{u}_z = \partial\mathbf{p}_e/\partial t$, where $\mathbf{p}_e = p_e(t)\mathbf{u}_z$ is the electric-dipole moment of the source [27].

In what follows the VED is assumed to be located directly on the graphene sheet (i.e., at $z_0 = 0$) in order to maximize its interaction with the SPP field, which is typically confined in the close proximity of the sheet. This choice also simplifies somewhat the subsequent analytical developments; however, the general case of a source placed at a nonzero distance from the sheet could be treated equally well with the same approach.

B. Electromagnetic model of graphene

As concerns the graphene sheet, this can generally be modeled in the spectral domain as a conductive sheet with a 2×2 dyadic surface conductivity [28]. The dyadic form is due to the application of a magnetostatic bias together with a nonzero chemical potential μ_c and/or to spatial-dispersion effects [29,30]. As in Ref. [22], we will not consider the presence of magnetic biasing fields and we will neglect the role of spatial dispersion, since it has been shown that for isolated graphene sheets nonlocal effects are unimportant, at least below the high-THz range [31].

In such a case, the infinite graphene sheet can be modeled in the FD through a local scalar two-dimensional (2D) conductivity σ_g [S], which mainly depends on the radian frequency $\omega = 2\pi f$ and a phenomenological scattering rate $\Gamma = 1/\tau_s$ (where τ_s is the relaxation time depending on a variety of factors and determined experimentally) [32], in addition to the chemical potential μ_c. In particular, at room temperatures and for frequencies below the low-THz regime, where interband terms can also be neglected, the conductivity has a Drude-like dispersion behavior,

$$\sigma_g(\omega) = \frac{\chi}{\Gamma + j\omega} = \frac{\sigma_0}{1 + j\omega/\Gamma}, \tag{1}$$

where j is the imaginary unit, $\sigma_0 = \chi/\Gamma$ is the graphene dc conductivity, and

$$\chi = \frac{q_e^2 k_B T}{\pi\hbar^2}\ln\left\{2\left[1 + \cosh\left(\frac{\mu_c}{k_B T}\right)\right]\right\}, \tag{2}$$

with $-q_e$ the electron charge, $\hbar$ the reduced Planck constant, k_B the Boltzmann constant, and T the absolute temperature. Actually, as also shown in Ref. [23], the consideration of interband terms (whose effects are dominant starting from the high-THz regime) produces negligible effects in the TD Green's function of the problem. The consideration of only the intraband conductivity as in (1) is thus not a limiting assumption for the subsequent developments.

The electromagnetic model of graphene can thus be expressed in the FD by enforcing the continuity of the tangential electric field $\mathbf{E}_\tau$ across the graphene sheet and relating such a field to the jump of the tangential magnetic field through a surface (transition) impedance boundary condition:

$$\begin{aligned}&\mathbf{E}_\tau(x,y,z = 0^+,\omega) = \mathbf{E}_\tau(x,y,z = 0^-,\omega),\\ &\mathbf{E}_\tau(x,y,z = 0,\omega) = Z_g(\omega)[\mathbf{u}_z \times \mathbf{H}_\tau(x,y,z = 0,\omega)]^+_-,\end{aligned} \tag{3}$$

where $Z_g(\omega)$ is the graphene surface impedance [Ω], with

$$Z_g(\omega) = R_g + j\omega L_g = \frac{1}{\sigma_g(\omega)} = \frac{1}{\sigma_0} + j\omega\frac{1}{\chi}, \tag{4}$$

i.e., $R_g = 1/\sigma_0$, $L_g = 1/\chi$.

C. Frequency- and time-domain fields

The considered source excites a field purely transverse magnetic with respect to the z axis (TM^z). Thanks to the rotational symmetry of the configuration around the z axis, the field is also

azimuthally symmetric, with nonzero cylindrical components $e_\rho(\rho,z,t)$, $e_z(\rho,z,t)$ of the electric field and $b_\phi(\rho,z,t)$ of the magnetic induction. In what follows we focus in particular on the magnetic induction observed at a point P along the graphene sheet, i.e., at $z=0$ (see Fig. 1), written concisely as $b_\phi(\rho,t)$.

The total magnetic induction $b_\phi(\rho,t)$ can be decomposed into incident and reflected components, $b^{\rm i}_\phi(\rho,t)$ and $b^{\rm r}_\phi(\rho,t)$, respectively:

$$b_\phi(\rho,t) = b^{\rm i}_\phi(\rho,t) + b^{\rm r}_\phi(\rho,t). \tag{5}$$

The former is the field produced by a transient dipole in free space, i.e., in the absence of graphene, and its expression is available in a closed analytical form [see, e.g., Ref. [33], Eq. 3(c)]:

$$b^{\rm i}_\phi(\rho,t) = \frac{\mu_0}{4\pi\rho}\left[s_0 p''_{\rm e}(t^*) + \frac{1}{\rho}\,p'_{\rm e}(t^*)\right]_{t^*=t-s_0\rho}, \tag{6}$$

where the prime $'$ indicates derivation with respect to the retarded time t^*.

As concerns the reflected field, as is well known its FD counterpart $B^{\rm r}_\phi(\rho,\omega)$ can be cast in the form of an inverse Hankel (or Fourier-Bessel) transform of order 1 [34]:

$$B^{\rm r}_\phi(\rho,\omega) = \int_0^\infty k_\rho J_1(k_\rho\rho)\tilde{B}^{\rm r}_\phi(k_\rho,\omega)\,dk_\rho, \tag{7}$$

where k_ρ is the radial wave number; $J_1(\cdot)$ is the Bessel function of first kind and of order 1; and the spectral reflected field, denoted with a tilde, is

$$\tilde{B}^{\rm r}_\phi(k_\rho,\omega) = \frac{j\mu_0}{4\pi}\,I(\omega)\ell\,\frac{k_\rho}{k_z(k_\rho,\omega)}\,R(k_\rho,\omega). \tag{8}$$

Here $k_z=\sqrt{k_0^2-k_\rho^2}$ is the vertical wave number, where $k_0=\omega s_0$ is the free-space wave number; $I(\omega)$ is the Fourier transform of the source current wave form $i(t)$; and finally, the spectral TM reflection coefficient R is

$$R(k_\rho,\omega) = -\frac{k_z(k_\rho,\omega)}{2\omega s_0\bar{Z}_{\rm g}(\omega)+k_z(k_\rho,\omega)} \tag{9}$$

(where the overbar indicates normalization with respect to the free-space impedance $\eta_0=\sqrt{\mu_0/\varepsilon_0}$) [34]. By inserting (9) into (8) we have

$$\tilde{B}^{\rm r}_\phi(k_\rho,\omega) = -\frac{j\mu_0}{4\pi}\,I(\omega)\ell\,\frac{k_\rho}{2\omega s_0\bar{Z}_{\rm g}(\omega)+k_z(k_\rho,\omega)}. \tag{10}$$

The integration in (7) can customarily be extended to the entire real axis by expressing the Bessel function $J_1(\cdot)$ in terms of the Hankel functions $H_1^{(1,2)}(\cdot)$ and exploiting the appropriate analytic-continuation properties [35], thus obtaining

$$B^{\rm r}_\phi(\rho,\omega) = \frac{1}{2}\int_{-\infty}^\infty k_\rho H_1^{(2)}(k_\rho\rho)\tilde{B}^{\rm r}_\phi(k_\rho,\omega)\,dk_\rho. \tag{11}$$

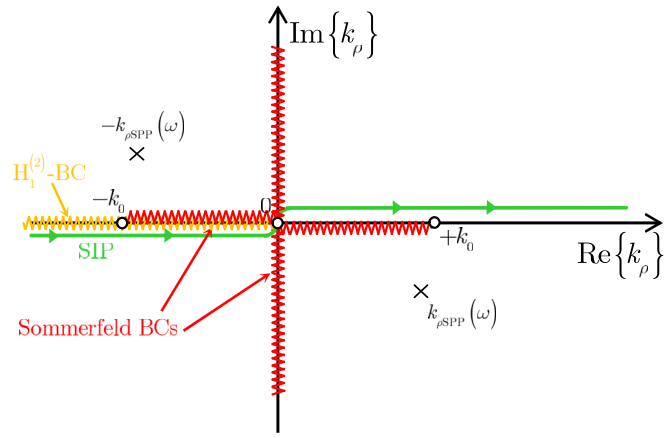

FIG. 2. Sommerfeld integration path (SIP) for the calculation of the FD field B_ϕ as an inverse Hankel transform of order 1. The singularities of the spectral field are also indicated: branch points at $k_\rho=\pm k_0$ (circles), associated with the determination of the vertical wave number k_z, and the relevant Sommerfeld branch cuts (red wiggly lines); branch point at $k_\rho=0$ (circle), associated with the Hankel function $H_1^{(2)}(\cdot)$, and the relevant branch cut (orange wiggly line); and poles at $k_\rho=\pm k_{\rho\rm SPP}(\omega)$ (crosses), associated with FD SPP modes.

Note that the integration path in (11), usually known as the Sommerfeld integration path (SIP), should lie infinitesimally above/below the branch points, located on the real axis at at $k_\rho=\pm k_0$, introduced by the square-root function that defines the vertical wave number k_z. (See Fig. 2, where the associated standard Sommerfeld branch cuts defined by $\mathrm{Im}\{k_z^2\}=0$, $\mathrm{Re}\{k_z^2\}\geqslant 0$ are also reported [34].) For definiteness, in what follows the symbol k_z will indicate the *proper* determination of the vertical wave number, i.e., the one with $\mathrm{Im}\{k_z\}\leqslant 0$. [Note that the Hankel function $H_1^{(2)}(\cdot)$ introduces an additional logarithmic branch point at $k_\rho=0$; the associated branch cut is customarily chosen to lie on the negative real axis of the k_ρ plane, with the SIP lying below it, and is devoid of physical meaning.]

In addition to these branch-point singularities, the integrand in (11) also has two pole singularities at $k_\rho=\pm k_{\rho\rm SPP}(\omega)$, associated with the well-known FD TM SPP mode supported by an isolated graphene sheet [8,16,18]. The FD SPP wave number $k_{\rho\rm SPP}(\omega)$ is a solution of the relevant TM dispersion equation

$$2\omega s_0\bar{Z}_{\rm g}(\omega)+k_z(k_\rho,\omega)=0, \tag{12}$$

obtained equating to zero, the denominator of (10), and can be expressed in a closed analytical form,

$$k_{\rho\rm SPP}(\omega) = \omega s_0\sqrt{1-4\bar{Z}_{\rm g}^2(\omega)}, \tag{13}$$

where the determination of the square root lying in the fourth quadrant of the k_ρ plane (i.e., the one with $\mathrm{Im}\{k_{\rho\rm SPP}\}<0$) will be assumed henceforth (see Fig. 2).

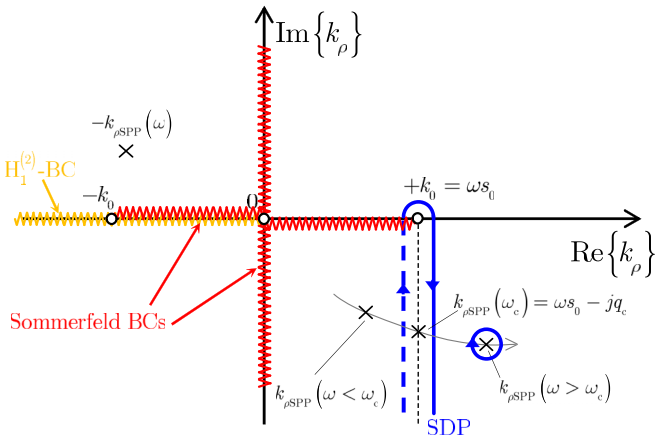

FIG. 3. Path deformation in the k_ρ plane: SDP through the branch point $k_\rho = k_0$ and evolution of the SPP pole $k_{\rho\mathrm{SPP}}$ as a function of the radian frequency ω.

Finally, the TD reflected field $b^{\mathrm{r}}_\phi(\rho,t)$ can be calculated by inverse Fourier transforming (11) with respect to time. Taking into account that TD quantities are real, such an inverse Fourier transform can be written as

$$b^{\mathrm{r}}_\phi(\rho,t) = \frac{1}{\pi}\,\mathrm{Re}\left\{\int_0^\infty B^{\mathrm{r}}_\phi(\rho,\omega)e^{j\omega t}\,d\omega\right\} = \mathrm{Re}\left\{\int_0^\infty\int_{-\infty}^\infty \frac{k_\rho}{2\pi}\,H_1^{(2)}(k_\rho\rho)\tilde{B}^{\mathrm{r}}_\phi(k_\rho,\omega)\,dk_\rho e^{j\omega t}\,d\omega\right\}. \tag{14}$$

In the next section the expression (14) for the TD reflected field will be manipulated using the DDT in order to single out the relevant TD SPP contribution.

III. DDT AND TIME-DOMAIN SPP FIELD

A. Summary of the DDT steps

The DDT is a two-step procedure based on sequential deformations of the k_ρ and ω integration paths that requires a careful analysis of the involved singularities of the integrands in the k_ρ and ω complex planes, respectively. A detailed exposition for the considered case of a graphene sheet in free space is given in the Appendixes A and B. Here a sketchy summary is given, aimed at providing the reader a quick route to the proposed expression for the TD SPP field.

The first step of the DDT consists in deforming the integration path of the inverse Hankel transform (11) into the lower half of the k_ρ plane from the SIP to the vertical SDP $k_\rho = k_0 - jq$ ($q \in \Re_0^+$) passing through the branch point $k_\rho = k_0 = \omega s_0$ (see Fig. 3). Note that the SDP is folded onto itself and lies partly on the proper Riemann sheet (solid line), partly on the improper sheet (dashed line).

The FD field can thus be represented as the sum of two contributions, $B_{\phi\mathrm{SPP}}(\rho,\omega)$ and $B_{\phi\mathrm{SDP}}(\rho,\omega)$, arising from the residue of the SPP pole $k_{\rho\mathrm{SPP}}$ and from the integration along the SDP, respectively. By inverse Fourier transforming with respect to time, we then have for the TD field

$$b^{\mathrm{r}}_\phi(\rho,t) = b'_{\phi\mathrm{SPP}}(\rho,t) + b_{\phi\mathrm{SDP}}(\rho,t), \tag{15}$$

where

$$b'_{\phi\mathrm{SPP}}(\rho,t) = \mathrm{Re}\left\{\int_{\omega_c}^\infty \frac{1}{2\pi}\,k_{\rho\mathrm{SPP}}(\omega)H_1^{(2)}[k_{\rho\mathrm{SPP}}(\omega)\rho] \times(-2\pi j)\mathrm{Res}[\tilde{B}^{\mathrm{r}}_\phi(k_\rho,\omega);k_{\rho\mathrm{SPP}}(\omega)]e^{j\omega t}\,d\omega\right\} \tag{16}$$

and

$$b_{\phi\mathrm{SDP}}(\rho,t) = \mathrm{Re}\left\{\int_0^\infty\int_{\mathrm{SDP}} \frac{k_\rho}{2\pi}\,H_1^{(2)}(k_\rho\rho) \times\tilde{B}^{\mathrm{r}}_\phi(k_\rho,\omega)\,dk_\rho e^{j\omega t}\,d\omega\right\}. \tag{17}$$

Note that, as shown in Appendix A, when $\omega = \omega_c$ the FD SPP pole crosses the SDP at $k_\rho = \omega s_0 - jq_c$, with $\omega_c = \Gamma/\sqrt{1+4\bar{R}_g^2}$ and $q = q_c = 4s_0\bar{R}_g^2\omega_c^2/\Gamma$. Since the pole is captured in the path deformation only if $\omega > \omega_c$ (see Fig. 3), its residue contribution is zero if $\omega < \omega_c$. (This is why the lower integration limit of the ω integral in (16) has been set equal to ω_c.) As a consequence, the Fourier transform of (16) is identically zero for $\omega < \omega_c$ and hence it does not satisfy the well-known Paley-Wiener causality criterion (see, e.g., Ref. [36], p. 16, Theorem XII).

Therefore, (16) does not define a physical TD SPP field. As shown in Appendix B, this can be obtained instead by adding to (16) a second contribution, arising from a deformation of the integration path of (17) in the ω plane and making causal the resulting field.

To this aim, we first exchange the order of integrations in (17) and then deform the integration path of the inner ω integral from the positive real axis to the ω-SDP passing through the origin; this is the *positive* imaginary axis when $t > s_0\rho$, and the *negative* imaginary axis when $t < s_0\rho$ (see Fig. 4).

In this last deformation due care has to be taken, of course, of the various singularities of the integrand in the ω plane and of their evolution as a function of the outer integration variable q (i.e., the imaginary part of the k_ρ wave number along the k_ρ-SDP). A detailed analysis (reported in Appendix B) shows that the spectral Green's function of a graphene sheet in free space has *four* pole singularities in the ω plane. Of these, only one, denoted as $\omega_{\mathrm{SPP}}(q)$, crosses the positive real axis at $\omega = \omega_c$ when $q = q_c$ and can thus be associated with the FD SPP pole $k_{\rho\mathrm{SPP}}$; its evolution as a function of q is also reported in Fig. 4.

The resulting representation for $b_{\phi\mathrm{SDP}}$ can then be cast in the following form:

$$b_{\phi\mathrm{SDP}}(\rho,t) = b''_{\phi\mathrm{SPP}}(\rho,t) + b_{\phi\mathrm{SDP}^2}(\rho,t) + b_{\phi\mathrm{other}}(\rho,t), \tag{18}$$

where $b''_{\phi\mathrm{SPP}}(\rho,t)$ arises from the residue contribution of the pole $\omega_{\mathrm{SPP}}(q)$; $b_{\phi\mathrm{SDP}^2}(\rho,t)$ is a double-integral SDP contribution; and $b_{\phi\mathrm{other}}(\rho,t)$ arises from the contribution of other Green's function poles as well as of the ω singularities of the source spectrum $I(\omega)$ (if any).

We note that the above-described DDT-based approach is valid for any Fourier-transformable source wave form $i(t)$, provided that the relevant spectrum $I(\omega)$ allows for deforming the integration path in the ω plane from the positive real axis to the positive or negative imaginary axis with a zero contribution of the path at infinity. In particular, the wide class of wave

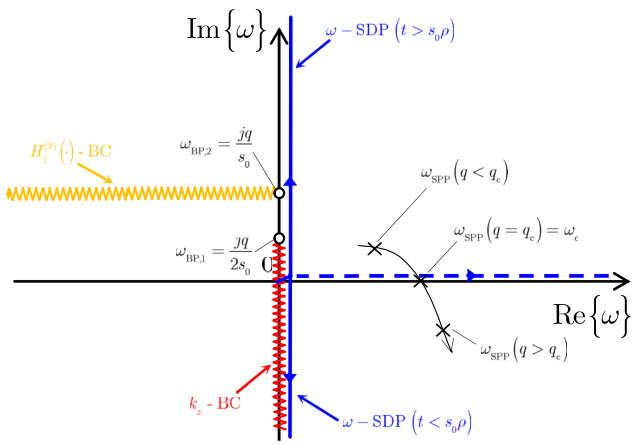

FIG. 4. Path deformation in the ω plane: SDPs through the origin for $t > s_0\rho$ (positive imaginary axis) and $t < s_0\rho$ (negative imaginary axis) and evolution of the SPP pole $\omega_{\rho\mathrm{SPP}}$ as a function of the imaginary part q of the radial wave number along the k_ρ-SDP ($k_\rho = k_0 - jq$). Two branch-point singularities are also shown with the relevant branch cuts, arising from the square-root function in the definition of the vertical wave number k_z and from the Hankel function $H_1^{(2)}(\cdot)$.

forms having support and integrable on the positive real axis can be considered, as well as Dirac δ functions. The proposed formalism is thus able to provide a representation for the TD Green's function of the considered configuration.

B. Time-domain SPP field

As shown in Appendix B, the total field, sum of the incident field (6) and of the DDT-based representation of the reflected field (15) with (18), is identically zero before the first wavefront arrival, i.e., for $t < s_0\rho$, as required by causality.

But even more is true. If we consider the two SPP-related terms $b'_{\phi\mathrm{SPP}}$ and $b''_{\phi\mathrm{SPP}}$, these are both different from zero; however, for $t < s_0\rho$ they are exactly equal and opposite. A *causal* TD SPP field can therefore be defined as

$$b_{\phi\mathrm{SPP}}(\rho,t) = b'_{\phi\mathrm{SPP}}(\rho,t) + b''_{\phi\mathrm{SPP}}(\rho,t), \tag{19}$$

i.e., summing the residue contributions of *two* pole singularities (not one, as for the usual FD SPP field).

The contribution $b'_{\phi\mathrm{SPP}}$ has clearly a modal nature since it is an (inverse Fourier) integral superposition of standard FD (SPP) modes. As concerns the contribution $b''_{\phi\mathrm{SPP}}$, such a term derives from $b_{\phi\mathrm{SDP}}$, i.e., from the inverse Fourier transform of the FD nonmodal space wave [26]. However, having interchanged the ω and q integrals and isolated the residue contribution of an ω pole (associated with the SPP k_ρ pole), it can be argued that $b''_{\phi\mathrm{SPP}}$ has a modal character as well, since it is an integral superposition of nonstandard TD modes [37].

As concerns the computational aspects, it is remarkable that for the case of a graphene sheet in free space, the involved k_ρ poles and ω poles can be determined in closed analytical forms, without the need of any root-searching procedure. Therefore, the evaluation of (19) reduces to the numerical calculation of two single integrals: an ω integral over the semi-infinite domain $[\omega_c, +\infty)$ ($b'_{\phi\mathrm{SPP}}$) and a q integral over the finite domain $[0, q_c]$ ($b''_{\phi\mathrm{SPP}}$).

IV. NUMERICAL RESULTS AND DISCUSSION

Numerical results will be presented in this section in order to (i) validate the proposed DDT-based representation of the total magnetic induction $b_\phi(\rho,t)$ excited by a VED on a graphene sheet in free space against independent computations; (ii) illustrate the significance of the various single DDT contributions to the total induction; and (iii) discuss the role of the TD SPP contribution for various spatiotemporal observation points.

The graphene sheet is modeled using (1) with $\tau = 0.5$ ps, $\mu_c = 0$ eV, and $T = 300$ K. For simplicity, a damped sine with radian frequency $\omega_0 = 2\pi/T_c$ and damping parameter $a > 0$ will be assumed here as a source wave form:

$$i(t) = I_0 e^{-at} \sin(\omega_0 t) u_{-1}(t), \tag{20}$$

where $u_{-1}(\cdot)$ is the Heaviside unit-step function, with T_c in the range from $\tau = 0.5$ ps to $10\tau = 5$ ps and $a = 2\omega_0/\pi$.

The only singularities of the relevant spectrum

$$I(\omega) = I_0 \frac{\omega_0}{(a + j\omega)^2 + \omega_0^2} \tag{21}$$

are a pair of poles, located at $\omega = \pm\omega_{ps} = \pm\omega_0 + ja$ in the first and second quadrants of the complex ω plane.

The spectrum (21) is almost flat from dc to the frequency $f_0 = \omega_0/(2\pi)$ (beyond which it rapidly approaches the asymptotic decay $\sim 1/\omega$). For the considered values of T_c it results $f_{0\max} = 2$ THz; hence, spatial-dispersion and interband terms can be neglected in the graphene conductivity expression, which can thus be correctly represented by (1). On the other hand, it results $f_{0\min} = 100$ GHz, so that for all the considered values of T_c the spectral content of the source is not negligible above the SPP cutoff frequency $f_c = \omega_c/(2\pi) \simeq 117$ GHz and thus the source is capable of exciting appreciably the TD SPP.

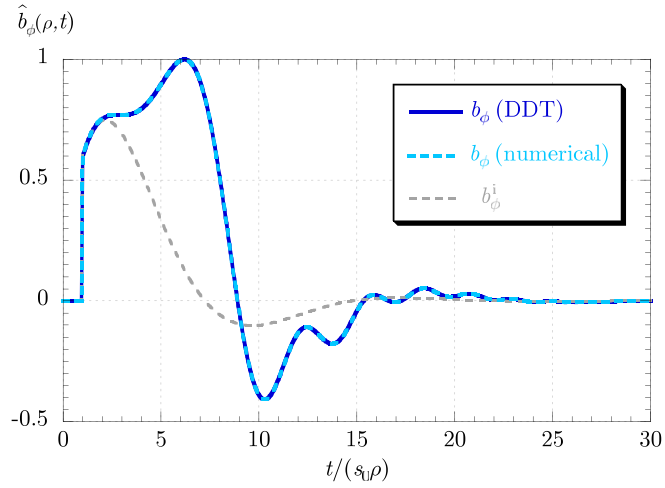

FIG. 5. Normalized time-domain magnetic induction $\hat{b}_\phi(\rho,t)$ as a function of the normalized time $t/(s_0\rho)$: comparison between our formulation (blue solid line) and a brute-force numerical inversion of the relevant spectral induction (cyan dashed curve). The incident induction is also reported for reference (gray dashed curve). Parameters: $\rho = 0.1$ mm, $T_c = 5$ ps.

The incident magnetic induction produced by a VED with current wave form (20) is, from (6),

$$b_\phi^{\mathrm{i}}(\rho,t) = b_0(\rho)e^{-at}\sin[\omega_0 t + \phi_b(\rho)]u_{-1}(t), \tag{22}$$

where

$$b_0(\rho) = \frac{\mu_0 I_0 \ell}{4\pi\rho}\sqrt{\left(\frac{1}{\rho} - as_0\right)^2 + \omega_0^2 s_0^2} \tag{23}$$

and

$$\phi_b(\rho) = \arctan\left(\frac{\omega_0 s_0 \rho}{1 - as_0\rho}\right). \tag{24}$$

A. Validation

In Fig. 5 the normalized time-domain magnetic induction $\hat{b}_\phi(\rho,t)$ (where the hat indicates normalization to $\max\{|b_\phi(\rho,t)|\}$) is reported as a function of the normalized time $t/(s_0\rho)$ for $\rho = 0.1$ mm and a current profile as in (20) with $T_c = 5$ ps. The induction is calculated both with our formulation (*blue solid line*) and with a purely numerical evaluation of its double inverse Fourier/Hankel representation (14) (cyan dashed line). The two curves are perfectly superimposed.

As a further validation, the same configuration as in Fig. 5 is considered, using as a source wave form the damped sinusoidal function (20) multiplied times t. The DDT formulation remains unchanged, except for the contribution $\hat{b}_{\phi\mathrm{ps}}(\rho,t)$, which now derives from a double pole at ω_{ps} whose residue has a more elaborate expression (not reported here for brevity). In this case the total induction is continuous at $t = s_0\rho$ (i.e., at the time of the first wave-front arrival) and a simulation with the electromagnetic simulation software CST MICROWAVE STUDIO is thus feasible [38]. This software discretizes the time-domain integral form of Maxwell's equations in a three-dimensional region by using the finite integration technique (FIT); a perfectly matched layer (PML) has been included here to terminate the computational domain. As can be seen in Fig. 6, the agreement between our DDT-based formulation and both the brute-force numerical inversion and the results obtained with CST is again excellent; note that to obtain convergence, tens of millions of cells have been employed in the CST simulation.

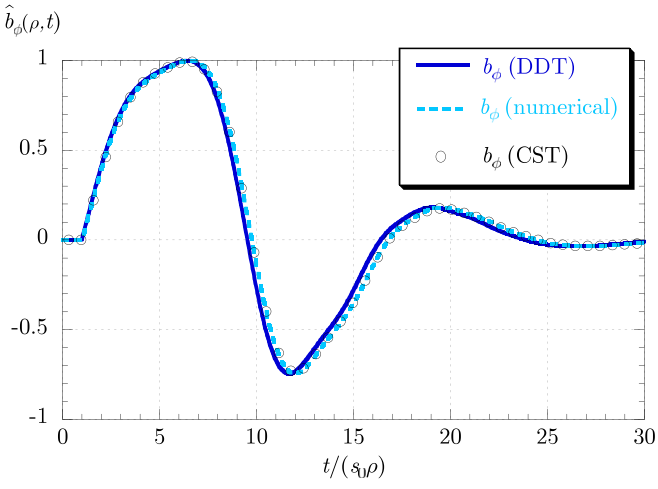

FIG. 6. Normalized time-domain magnetic induction $\hat{b}_\phi(\rho,t)$ as a function of the normalized time $t/(s_0\rho)$: comparison between our formulation (blue solid line), a brute-force numerical inversion of the relevant spectral induction (cyan dashed curve), and results obtained with CST (black circles). Parameters: As in Fig. 5, with a source wave form multiplied by t.

B. DDT constituents of the TD wave form

In Fig. 7 $\hat{b}_\phi(\rho,t)$ and its constituent parts according to (B14), (B15) are reported as functions of the normalized time $t/(s_0\rho)$ for $\rho = 0.1$ mm and current profile as in (20) with $T_c = \tau = 0.5$ ps. The incident field can be seen from Fig. 7(a) to be dominant for early times. However, for $t/(s_0\rho) > 3$ it rapidly becomes negligible [see Fig. 7(b)], while the TD SPP field $b_{\phi\mathrm{SPP}}$ simultaneously becomes the dominant contribution to the reflected field. In particular, for this choice of parameters the TD SPP is almost completely given by the term $b'_{\phi\mathrm{SPP}}$ alone. Note, however, that $b'_{\phi\mathrm{SPP}}$ and $b''_{\phi\mathrm{SPP}}$ are equal and opposite for $t/(s_0\rho) < 1$, i.e., before the arrival of the first wave front,

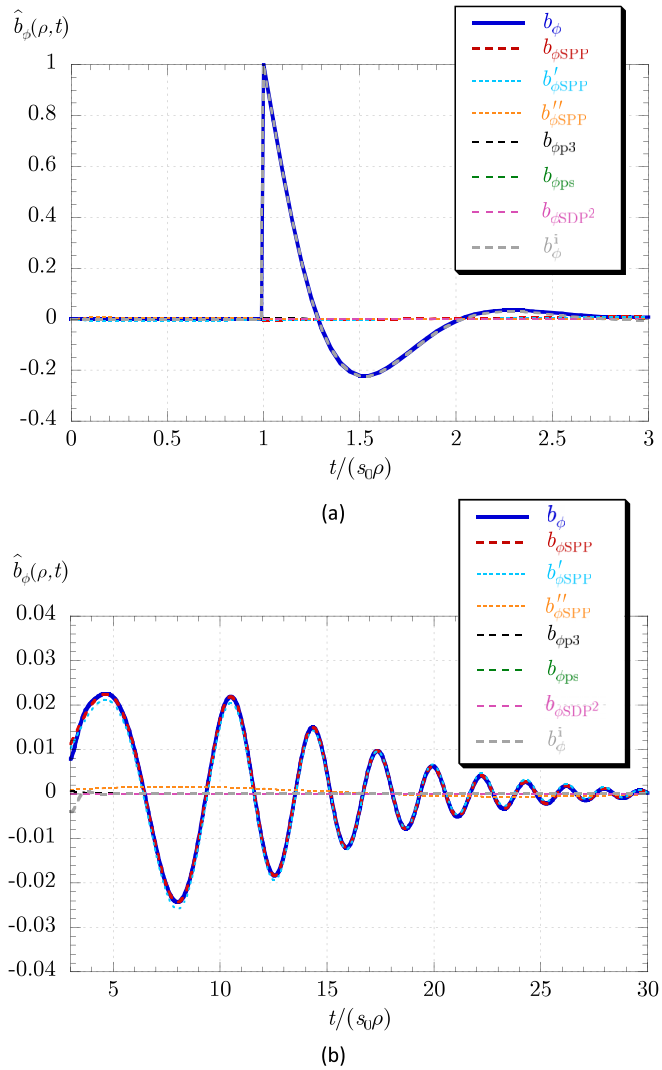

FIG. 7. Normalized time-domain magnetic induction and its constituent parts as functions of the normalized time $t/(s_0\rho)$ for $\rho = 0.1$ mm and current profile as in (20) with $T_c = 0.5$ ps: (a) $0 < t/(s_0\rho) < 3$ and (b) $t/(s_0\rho) > 3$.

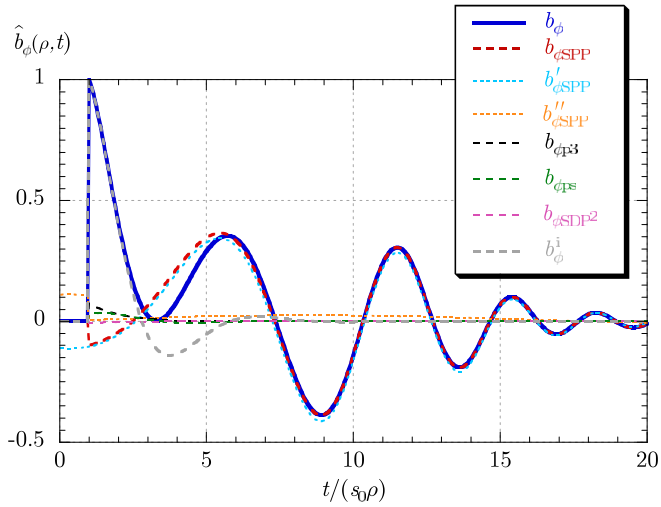

FIG. 8. Same as in Fig. 7 for $T_c = 2$ ps (a) and $T_c = 5$ ps (b).

as required to have a causal response. As concerns the other contributions, i.e., $b_{\phi SDP}$, $b_{\phi p3}$, and $b_{\phi ps}$, they are negligible for all times. (Although not shown here, the SDP term could be seen to give an appreciable though modest contribution to the reflected field for very early times; however, this cannot be observed in the total field, which is dominated by the incident field at those times.)

By increasing the characteristic time T_c of the source wave form beyond the collision time τ of the graphene sheet, the source spectrum shrinks to lower frequencies, where the Drude-like graphene conductivity (1) is higher in absolute value and hence the graphene sheet is more reflective. Accordingly, the reflected field gradually gains significance with respect to the incident field, as can be observed in Figs. 8(a) and 8(b), where the values $T_c = 4\tau = 2$ ps and $T_c = 10\tau = 5$ ps are considered, respectively. On the other hand, now the incident field decays more slowly and hence, after being dominant for early times, remains non-negligible for a larger time interval. It can also be observed that by increasing T_c, the TD SPP term $b_{\phi SPP}$ tends to become dominant at larger

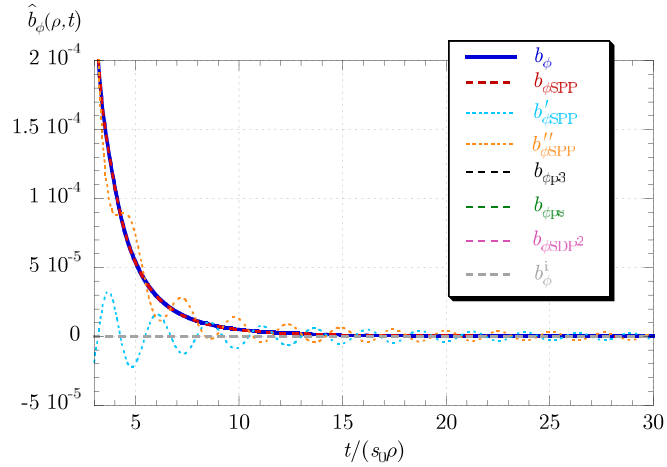

FIG. 9. Normalized time-domain magnetic induction and its constituent parts as functions of the normalized time $t/(s_0\rho)$ for $\rho = 1$ mm and current profile as in (20) with $T_c = 1$ ps.

times, with the contribution $b''_{\phi SPP}$ gradually increasing relative importance with respect to $b'_{\phi SPP}$.

By increasing the observation distance ρ, however, the situation changes. For instance, in Fig. 9 the case $\rho = 1$ mm is considered, with $T_c = 2\tau = 1$ ps. Again, the incident field is dominant for early times (not reported here). For late times the TD SPP field becomes dominant, but now its main constituent is the term $b''_{\phi SPP}$, which can be seen to oscillate synchronously and in phase opposition with respect to $b'_{\phi SPP}$.

The role of the various DDT contributions to the total field indeed changes by varying the observation distance ρ, as it can be more clearly appreciated from Fig. 10, where they are reported in normalized form and in absolute value as a function of ρ in the range from 0.01 to 10 mm, at a time t equal to a fixed multiple of the wave-front arrival time $s_0\rho$.

In particular, in Fig. 10(a) the case $t = 3s_0\rho$ is considered. It can be seen that for $\rho < 0.07$ mm the total field is dominated by the incident field. For ρ between 0.07 and 0.2 mm the incident and TD SPP field are comparable, and for $\rho > 0.2$ mm the TD SPP field is dominant. As concerns the TD SPP, the term $b'_{\phi SPP}$ is dominant for $\rho < 0.2$ mm, whereas $b''_{\phi SPP}$ becomes dominant for $\rho > 0.5$ mm. Finally, the terms $b_{\phi SDP}$, $b_{\phi p3}$, and $b_{\phi ps}$ are negligible for all ρ (although the latter two are much larger than the first one for small ρ).

By increasing the observation time to $t = 7s_0\rho$, it can be seen in in Fig. 10(b) that the incident field is always negligible except extremely close to the source, the TD SPP field becoming dominant already at $\rho > 0.04$ mm. However, now the TD SPP field is dominated by $b'_{\phi SPP}$ up to $\rho = 0.2$ mm, so that this term accurately represents the total field in the range from 0.04 to 0.2 mm. From 0.2 to 1 mm $b'_{\phi SPP}$ and $b''_{\phi SPP}$ are comparable; finally, for $\rho > 1$ mm the latter term becomes dominant and accurately represents the TD SPP (and hence the total) field.

C. Discussion

From the results reported in Figs. 7–10 the following general remarks can be made.

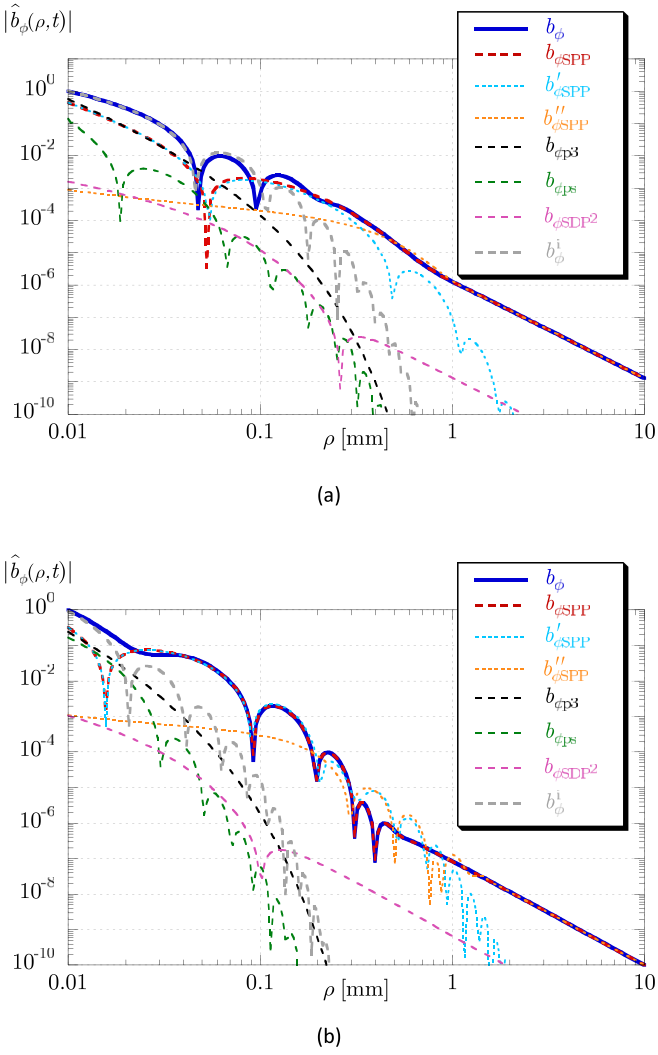

FIG. 10. Absolute value of the normalized time-domain magnetic induction and its constituent parts in a logarithmic scale as functions of ρ with and current profile as in (20) with $T_c = 1$ ps for $t = 3s_0\rho$ (a) and $t = 7s_0\rho$ (b).

First, the TD SPP field consistently provides an excellent representation for the reflected field observed at points on the graphene sheet (except for very early times).

Second, for a fixed observation point the TD SPP field also provides a very accurate representation of the total field at late times, i.e., when the incident field has decayed to negligible values. The exact definition of such a time frame depends on the characteristics of the source wave form, in particular, on its spectral occupancy in relation to the Drude-like spectrum of the graphene conductivity.

Third, there is a complex interplay between the two constituents of the TD SPP, namely, $b'_{\phi\mathrm{SPP}}$ and $b''_{\phi\mathrm{SPP}}$, whose relative importance depends on both the observation point and time. Before the first wave-front arrival, they are equal and opposite, as already observed. After that, their weight depends on the observation distance, $b'_{\phi\mathrm{SPP}}$ being dominant for small distances, $b''_{\phi\mathrm{SPP}}$ for large distances.

In order to discuss the physical implications of these findings, in Fig. 11 "phase diagrams" are reported, showing the main character of the transient field as a function of time

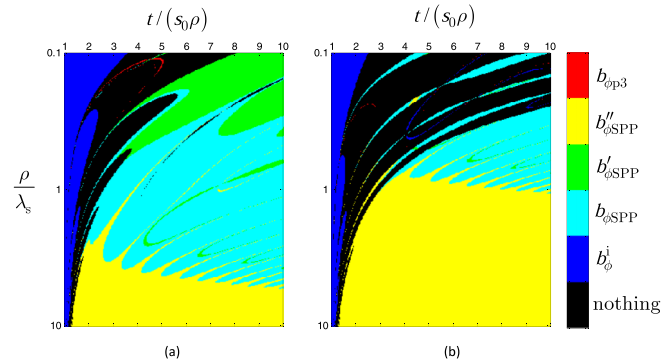

FIG. 11. "Phase diagrams" showing the main character of the transient field as a function of the normalized time $t/(s_0\rho)$ (horizontal axis) and normalized radial distance ρ/λ_s, with $\lambda_s = cT_c$ (vertical axis, logarithmic scale): (a) case of $T_c = 1$ ps and (b) case of $T_c = 5$ ps.

(normalized to the first wave-front arrival $s_0\rho$) and radial distance (normalized to the free-space wavelength $\lambda_s = cT_c$ corresponding to the oscillation frequency of the source) for the cases $T_c = 1$ and 5 ps.

In these diagrams, which provide a possible TD counterpart of those reported in Fig. 5 of Ref. [15], each pixel has a color corresponding to the field component that is dominant at the corresponding space-time location, according to the code reported in the vertical color bar on the right. The criterion for dominance of a component $b_{\phi,n}$ of the total induction b_ϕ has been chosen as $|b_\phi - b_{\phi,n}| < 0.1|b_\phi|$; if no component satisfies such a criterion, the black color has been used. Note that no color has been attributed to $b_{\phi\mathrm{SDP}^2}$ nor to $b_{\phi\mathrm{ps}}$, since they are never dominant.

A number of interesting observations can be made by examining Fig. 11 and the relevant field values. First, it can be noted that the incident field is dominant immediately after the first wave-front arrival, in a time interval whose length decreases with the distance from the source. Second, for larger distances and after a transition time interval in which there is not a clearly dominant component, the field is essentially dominated by the TD SPP [for small distances from the source this occurs for times larger than the range shown in Fig. 11(b)], in particular, as already noted, by $b'_{\phi\mathrm{SPP}}$ for large radial distances, by $b''_{\phi\mathrm{SPP}}$ for small distances, and by a combination of the two for intermediate distances. Third, when the TD SPP dominates, the magnitude of the field is considerably enhanced with respect to that of the incident field, of the order of 10^2 or more depending on the observation time.

As concerns the physics of these findings, we may conclude that the time-domain scenario in terms of dominance of the plasmonic field as well as of enhancement with respect to the incident, free-space field is very different from the one in the time-harmonic case.

In fact, in the low-terahertz range considered here, the field excited by a time-harmonic vertical dipole has the following main properties [15]: (1) In a core region close to the emitter, of the order of about ten propagation lengths $L_p = 1/\mathrm{Im}\{k_{\rho\mathrm{SPP}}\}$, the field is dominated by the frequency-domain SPP. Furthermore, in this region it is greatly enhanced in magnitude with respect to the incident, free-space field. (2) Outside such a core

region and after a short transition region, the field is essentially equal to the incident field. Because of (1), radiation/matter interaction can be greatly enhanced in the core region close to the source (leading to, e.g., high Purcell factors and other notable effects) [1].

In contrast, for the TD field excited by a transient vertical dipole, the TD SPP is never dominant for early times. When it becomes dominant, it does produce a significant magnitude enhancement with respect to the incident field; however, when this happens, the amplitude has already considerably decayed with respect to its early time values. These considerations have a direct impact on the design of any experimental system aimed at realizing the transient interaction of matter with radiation inside subwavelength regions via SPP fields.

V. CONCLUSIONS

A time-domain analysis of transverse-magnetic surface plasmon polaritons excited on a freestanding graphene sheet by a vertical electric dipole has been carried out by means of the double-deformation technique. This approach allows for identifying a causal field associated with the surface plasmon pole singularities of the relevant spectral Green's function by pairing the contribution arising from the standard plasmon pole in the complex plane of the radial wave number with another contribution arising from an associated pole in the complex plane of the radian frequency. This can be contrasted with other time-domain techniques such as the Cagniard–de Hoop technique, which does not allow for sorting out the contribution of pole singularities and thus extract modal components from the total field, or the direct numerical inversion of the modal plasmon field in the frequency domain, which produces noncausal results.

The time-domain surface plasmon polariton thus defined has been shown to be the dominant contribution to the field reflected by the graphene sheet. This is a nontrivial result, as it has been shown that the direct inverse Fourier transform of the standard modal plasmon field, typically dominant in the frequency domain up to radial distances of several wavelengths from the source, may be nondominant or even negligible, depending on the chosen observation distance and time.

On the other hand, considering the total transient field, it has been found that the properties of dominance of the plasmonic field and the associated enhancement of the field magnitude with respect to the free-space case are quite different from those typical of the time-harmonic case, an indication that transient plasmonics requires specific time-domain investigations for the correct design and interpretation of the relevant experiments.

APPENDIX A: PATH DEFORMATION IN THE k_ρ PLANE

By deforming the integration path of the inverse Hankel transform (11) into the lower half of the k_ρ plane from the SIP to the vertical SDP $k_\rho = k_0 - jq$ ($q \in \Re_0^+$) passing through the branch point $k_\rho = k_0 = \omega s_0$ (see Fig. 3), the FD field can be represented as the sum of two contributions arising from the residue of the SPP pole $k_{\rho\mathrm{SPP}}$ and from the integration along the SDP, respectively:

$$B_\phi^{\mathrm{r}}(\rho,\omega) = B_{\phi\mathrm{SPP}}(\rho,\omega) + B_{\phi\mathrm{SDP}}(\rho,\omega). \tag{A1}$$

Regarding the first term, we have

$$B_{\phi\mathrm{SPP}}(\rho,\omega) = -\pi j k_{\rho\mathrm{SPP}}(\omega) H_1^{(2)}[k_{\rho\mathrm{SPP}}(\omega)\rho] \times \mathrm{Res}\big[\tilde{B}_\phi^{\mathrm{r}}(k_\rho,\omega); k_{\rho\mathrm{SPP}}(\omega)\big] u_{-1}(\omega-\omega_{\mathrm{c}}), \tag{A2}$$

where ω_{c} is the cutoff radian frequency of the FD SPP mode. This is defined as the radian frequency at which the SPP pole crosses the SDP (see Fig. 3), i.e., $k_{\rho\mathrm{SPP}}(\omega_{\mathrm{c}}) = \omega s_0 - jq_{\mathrm{c}}$, thus being captured in the path deformation only if $\omega > \omega_{\mathrm{c}}$. Both ω_{c} and q_{c} can be calculated in a closed form from (13)

$$\omega_{\mathrm{c}} = \frac{\Gamma}{\sqrt{1+4\bar{R}_{\mathrm{g}}^2}}, \qquad q_{\mathrm{c}} = \frac{4 s_0 \bar{R}_{\mathrm{g}}^2}{\Gamma}\omega_{\mathrm{c}}^2. \tag{A3}$$

The residue in (A2) can also be calculated explicitly:

$$\mathrm{Res}\big[\tilde{B}_\phi^{\mathrm{r}}(k_\rho,\omega); k_{\rho\mathrm{SPP}}(\omega)\big] = \frac{j\mu_0}{4\pi} I(\omega)\ell \frac{k_{\rho\mathrm{SPP}}(\omega)}{k_{z\mathrm{SPP}}(\omega)} \times \mathrm{Res}[R(k_\rho,\omega); k_{\rho\mathrm{SPP}}(\omega)] = -\frac{j\omega\mu_0}{2\pi} I(\omega)\ell s_0 \bar{Z}_{\mathrm{g}}(\omega), \tag{A4}$$

where $k_{z\mathrm{SPP}} = \sqrt{k_0^2 - k_{\rho\mathrm{SPP}}^2} = -2\omega s_0 \bar{Z}_{\mathrm{g}}$ [having used (12)], so that

$$B_{\phi\mathrm{SPP}}(\rho,\omega) = -\frac{\omega\mu_0 s_0}{2} I(\omega)\ell \bar{Z}_{\mathrm{g}}(\omega) k_{\rho\mathrm{SPP}}(\omega) H_1^{(2)}[k_{\rho\mathrm{SPP}}(\omega)\rho] \tag{A5}$$

for $\omega > \omega_{\mathrm{c}}$ and $B_{\phi\mathrm{SPP}}(\rho,\omega) = 0$ for $\omega < \omega_{\mathrm{c}}$.

Regarding the second term in (A1), we have

$$B_{\phi\mathrm{SDP}}(\rho,\omega) = \frac{1}{2}\int_0^\infty (\omega s_0 - jq) H_1^{(2)}[(\omega s_0 - jq)\rho] \times D(q,\omega)(-j)\, dq, \tag{A6}$$

where the function $D(q,\omega)$ is defined as the difference between the spectral fields on the top and bottom parts of the SDP, i.e.,

$$D(q,\omega) = \big[\tilde{B}_\phi^{\mathrm{r}}[k_\rho = \omega s_0 - jq,\omega]\big]_{\mathrm{Bottom}}^{\mathrm{Top}} = \frac{j\mu_0}{2\pi} I(\omega)\ell \frac{k_\rho k_z}{4\omega^2 s_0^2 \bar{Z}_{\mathrm{g}}^2(\omega) - k_z^2}\bigg|_{k_\rho = \omega s_0 - jq} = \frac{j\mu_0}{2\pi} I(\omega)\ell \frac{(\omega s_0 - jq)\sqrt{2j\omega s_0 q + q^2}}{4\omega^2 s_0^2 \bar{Z}_{\mathrm{g}}^2(\omega) - 2j\omega s_0 q - q^2}, \tag{A7}$$

having used

$$k_z = k_z(k_\rho = \omega s_0 - jq, \omega) = \sqrt{2j\omega s_0 q + q^2}. \tag{A8}$$

In order to illustrate the typical behavior of the SPP pole $k_{\rho\mathrm{SPP}} = \beta_{\rho\mathrm{SPP}} - j\alpha_{\rho\mathrm{SPP}}$ as a function of the radian frequency, numerical results are presented in Fig. 12 for the case study of a graphene sheet described by (1) with $\tau_{\mathrm{s}} = 0.5$ ps (hence $\Gamma = 2 \times 10^{12}$ rad/s), $\mu_{\mathrm{c}} = 0$ eV, and $T = 300$ K.

In Fig. 12(a) the root locus of the SPP pole is reported in the complex plane of the normalized radial wave number $\hat{k}_\rho = k_\rho/k_0$. The locus starts on the negative imaginary axis at $\hat{k}_\rho = -j\sqrt{4\bar{R}_{\mathrm{g}}^2 - 1} = -j2.309$. By increasing the radian frequency,

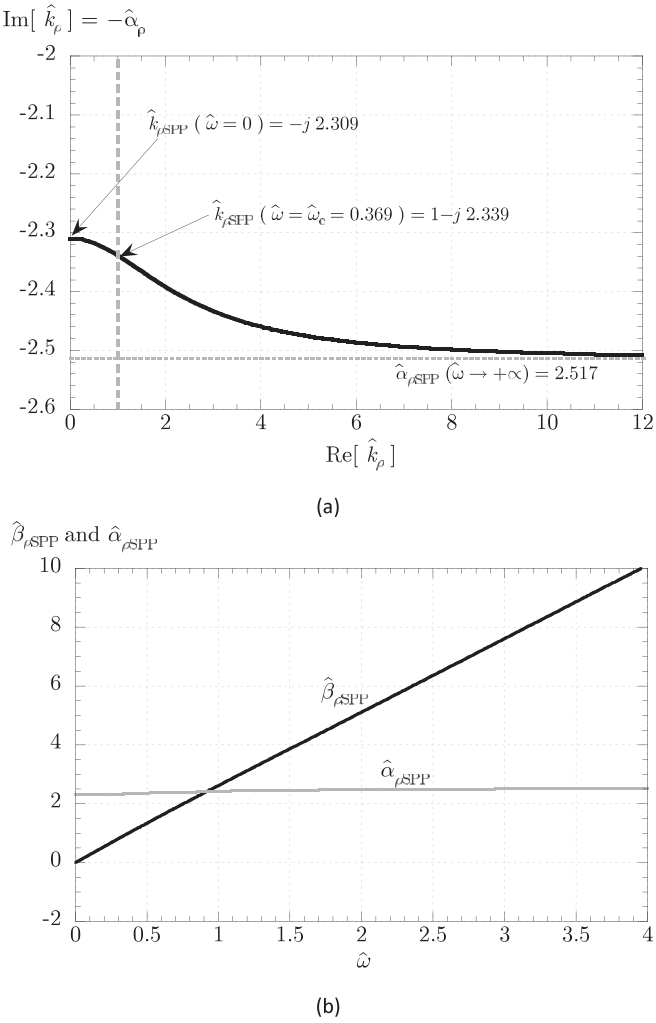

FIG. 12. SPP pole singularity $k_{\rho SPP} = \beta_{\rho SPP} - j\alpha_{\rho SPP}$ of the spectral field $\tilde{B}_\phi(k_\rho,\omega)$: (a) pole locus (blue line) in the complex plane of the normalized radial wave number $\hat{k}_\rho = k_\rho/k_0$, parameterized by the radian frequency ω; (b) the relevant dispersion curves for the normalized phase constant $\hat{\beta}_{\rho SPP}$ (black line) and attenuation constant $\hat{\alpha}_{\rho SPP}$ (red line). Parameters: $\tau_s = 0.5$ ps, $\mu_c = 0$ eV, $T = 300$ K.

both the normalized phase constant $\hat{\beta}_{\rho SPP}$ and the normalized attenuation constant $\hat{\alpha}_{\rho SPP}$ monotonically increase; the former has an asymptotically linear trend with frequency, whereas the latter tends to the limit value $\hat{\alpha}_{\rho SPP} = 2\bar{R}_g = 2.517$, as it can be observed in the dispersion plot reported in Fig. 12(b). The SDP is crossed at $\omega_c = 2\pi f_c = 0.369\Gamma$ (which corresponds to $f_c = 117$ GHz) with $\hat{\alpha}_{\rho SPP} = q_c/k_0 = 2.34$, in agreement with (A3).

APPENDIX B: PATH DEFORMATION IN THE ω PLANE

The TD field resulting at this stage is the sum of two contributions, obtained by inverse Fourier transforming (A1) with respect to time:

$$b^{\Gamma}_{\phi}(\rho,t) = b'_{\phi SPP}(\rho,t) + b_{\phi SDP}(\rho,t) \tag{B1}$$

where

$$b'_{\phi SPP}(\rho,t) = \frac{1}{\pi}\,\mathrm{Re}\left\{\int_0^\infty B_{\phi SPP}(\rho,\omega)e^{j\omega t}\,d\omega\right\} = \mathrm{Re}\left\{\int_{\omega_c}^\infty -\frac{\omega\mu_0 s_0}{2\pi}\,I(\omega)\ell k_{\rho SPP}(\omega)\bar{Z}_g(\omega) \times H_1^{(2)}[k_{\rho SPP}(\omega)\rho]e^{j\omega t}\,d\omega\right\} \tag{B2}$$

and

$$b_{\phi SDP}(\rho,t) = \frac{1}{\pi}\,\mathrm{Re}\left\{\int_0^\infty B_{\phi SDP}(\rho,\omega)e^{j\omega t}\,d\omega\right\} = \mathrm{Re}\left\{\int_0^\infty\int_0^\infty \frac{(\omega s_0 - jq)}{2\pi}\,H_1^{(2)}[(\omega s_0 - jq)\rho] \times D(q,\omega)(-j)\,dq e^{j\omega t}\,d\omega\right\}. \tag{B3}$$

As already noted in Sec. III, the first term is not causal. A causal TD SPP field can be obtained by adding to (B2) a second contribution, arising from a deformation of the integration path of (B3) in the ω plane and making causal the resulting field, as described in the following.

Considering then (B3), we first exchange the order of integrations, thus obtaining

$$b_{\phi SDP}(\rho,t) = \frac{1}{2\pi}\,\mathrm{Re}\left\{\int_0^\infty F(q)(-j)\,dq\right\} \tag{B4}$$

where

$$F(q) = \int_0^\infty (\omega s_0 - jq)H_1^{(2)}[(\omega s_0 - jq)\rho]D(q,\omega)e^{j\omega t}\,d\omega. \tag{B5}$$

The singularities of the integrand in (B5) are discussed next.

1. Singularities in the ω plane

The integrand of (B5) has pole singularities in the complex ω plane that arise from the zeros of the denominator of $D(q,\omega)$ in (A7). This is readily seen to be a fourth-order polynomial in ω; the relevant quartic equation can be written as

$$\hat{\omega}^4 - 2j\hat{\omega}^3 - \hat{\omega} + j\frac{\hat{q}}{2\bar{R}_g^2}\,\hat{\omega} + \frac{1}{4\bar{R}_g^2}\,\hat{q}^2 = 0 \tag{B6}$$

in terms of the normalized radian frequency $\hat{\omega} = \omega/\Gamma$ and the normalized wave number $\hat{q} = q/(s_0\Gamma)$. Equation (B6) has four roots, denoted as $\hat{\omega}_{p,i}$, $i = 1,2,3,4$, and parameterized by the normalized wave number $\hat{q}$. Importantly, such roots can be written explicitly as functions of the coefficients in (B6) and thus of $\hat{q}$ through the well-known Ferrari formulas (they are rather lengthy and thus are not reported here; see, e.g., Ref. [39]).

From (B6) it is seen that for $\hat{q} = 0$ we have two double roots, one at $\hat{\omega} = 0$ and one at $\hat{\omega} = j$. By increasing $\hat{q}$, the former double root splits into two distinct complex roots $\hat{\omega}_{p,i}$, $i = 1,2$, symmetrical with respect to the imaginary axis (see Fig. 13, where the pole loci $\hat{\omega}_{p,i}(q)$ are reported for the same case study considered in Fig. 12). These cross the real axis at $\hat{\omega} = \pm\hat{\omega}_c$ when $\hat{q} = \hat{q}_c$. Therefore, and this is a crucial point, we can associate the solution $\hat{\omega}_{p,1}$, i.e., the one crossing the positive

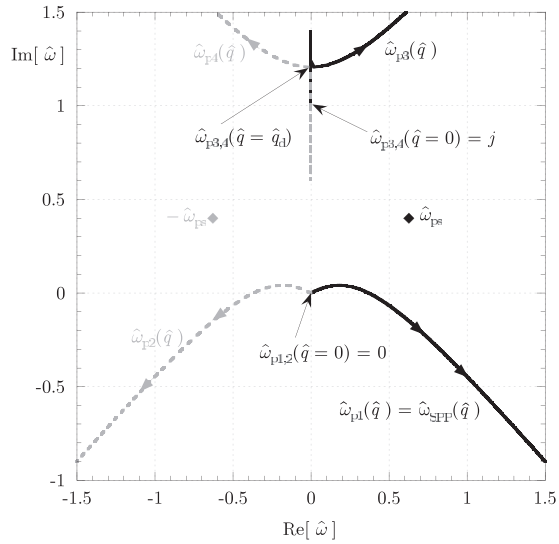

FIG. 13. Pole singularities in the complex plane of the normalized radian frequency $\hat{\omega}$: pole loci $\hat{\omega}_{p,i}$ $(i = 1,2,3,4)$, parameterized by the imaginary part q of the radial wave number on the SDP $k_\rho = \omega s_0 - jq$, and poles of the source spectrum $\pm\omega_{ps}$ (black and gray diamonds), independent of q. The graphene conductivity has parameters as in Fig. 12. Source parameters: $T_c = 20$ ps, $a = 4/T_c$.

real axis, with the SPP modal solution examined in the previous section, which crosses the SDP at $\hat{q} = \hat{q}_c$ when $\hat{\omega} = \hat{\omega}_c$.

As concerns the second pair of solutions $\hat{\omega}_{p,i}$, $i = 3,4$, by increasing q this splits from $\hat{\omega} = j$ remaining first on the real axis and moving in opposite directions. Then they invert their direction, coalescing again at $\hat{q} = \hat{q}_d$ into a double solution, which then splits into two complex solutions, symmetrical with respect to the imaginary axis (see Fig. 13).

The dynamics of the ω poles can be further appreciated from the curves in Fig. 14, where the real and imaginary parts of $\hat{\omega}_{p,i}$, $i = 1,2$ [Fig. 14(a)] and $i = 3,4$ [Fig. 14(b)] are reported as a function of $\hat{q}$.

In addition to the four poles discussed so far, there may be additional singularities arising from the source spectrum function $I(\omega)$. Assuming a damped sine as in (20), the relevant spectrum (21) has only a pair of poles in the first and second quadrants of the complex ω plane, also shown in Fig. 13 for the case $T_c = 20$ ps, $a = 2\omega_0/\pi = 4/T_c$.

The integrand of (B5) has also two branch-point singularities. The first one arises from the square-root function (A8) that defines the vertical wave number in the numerator of $D(q,\omega)$. The relevant branch point is thus located at $\omega_{BP,1} = jq/(2s_0)$, i.e., at $\hat{\omega}_{BP,1} = j\hat{q}/2$, and, having agreed to choose the proper determination of such a square-root function, the associated branch cut lies along the imaginary axis below $\omega_{BP,1}$. The second branch point is due to the Hankel function $H_1^{(2)}(\cdot)$ and occurs at $\omega s_0 - jq = 0$, i.e., at $\hat{\omega}_{BP,2} = j\hat{q}$; by choosing as is customary the associated branch cut along the negative real axis of the argument of the Hankel function, the resulting branch cut in the ω plane lies entirely in the second quadrant running parallel to the negative real axis.

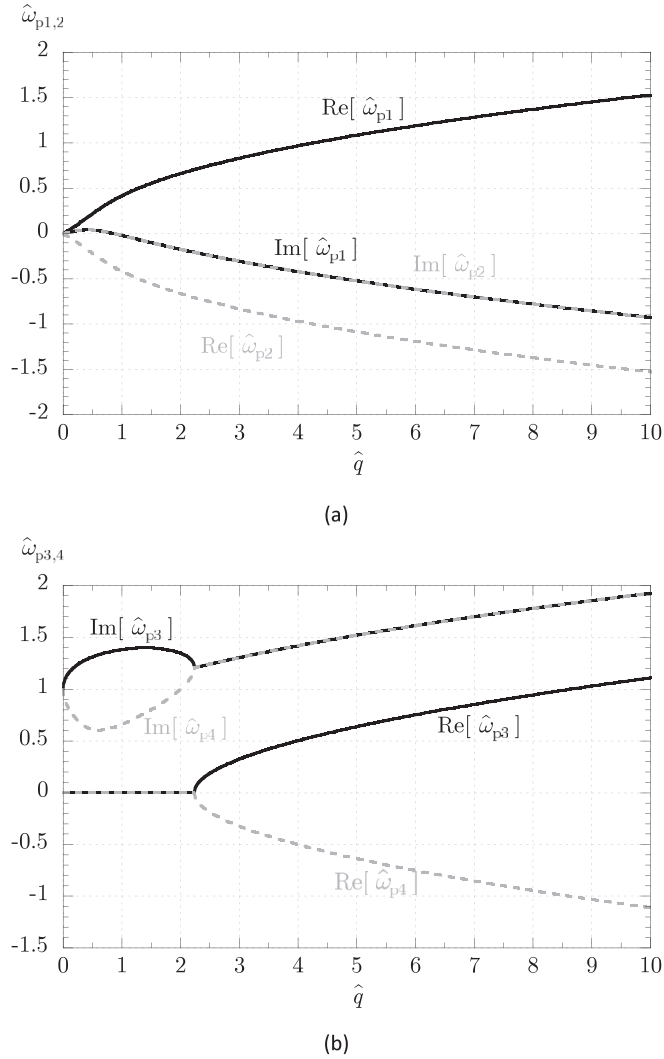

FIG. 14. Pole singularities in the complex plane of the normalized radian frequency $\hat{\omega}$: real and imaginary parts of $\hat{\omega}_{p,i}$ as functions of the normalized imaginary part $\hat{q}$ of the radial wave number on the SDP $k_\rho = \omega s_0 - jq$: (a) $i = 1,2$ and (b) $i = 3,4$.

2. Complete time-domain field

On the basis of the previous discussion of the involved ω-plane singularities, it is now possible to derive an alternative representation for (B4) via deformation to the ω-SDP passing through the origin. From the asymptotic behavior of the Hankel function for large arguments $H_1^{(2)}(z) \approx j^{3/2}\exp(-jz)\sqrt{2/(\pi z)}$, we deduce that the integrand in (B5) has an exponential term of the form $\exp[j\omega(t - s_0\rho)]\exp(-q\rho)$. Therefore, the ω-SDP will lie along the *positive* imaginary axis when $t > s_0\rho$ and on the *negative* imaginary axis when $t < s_0\rho$.

Note that, excluding the above-mentioned exponential and the source term $I(\omega)$, the remaining part of the ω integrand decays algebraically as $1/\omega^2$ at infinity in both the first and second quadrants. Therefore, Jordan's lemma allows for concluding that the contribution of the closing contour at infinity is zero, provided that $I(\omega)/\omega^2$ is infinitesimal at infinity. This accommodates a wide class of source wave forms $i(t)$,

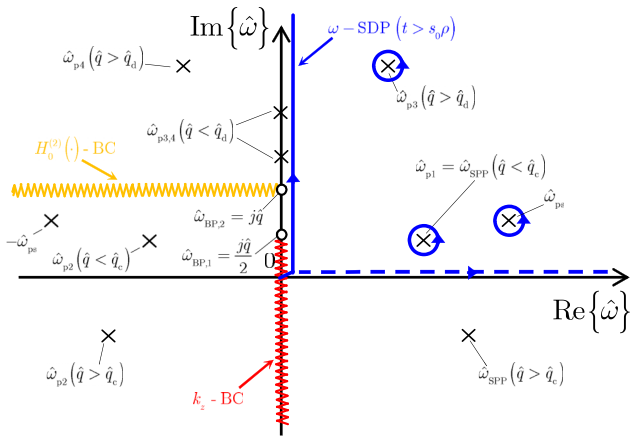

FIG. 15. Path deformation in the complex plane of the normalized radian frequency $\hat{\omega} = \omega/\Gamma$ from the positive real axis (dashed line) to the vertical SDP through the origin (solid line), for $t > s_0\rho$. The poles (crosses) and the BPs (circles) with the relevant BCs (wiggly lines) are also indicated.

including those having support and integrable on the positive real axis, whose spectrum is infinitesimal at infinity, as well as Dirac δ's, whose spectrum is constant.

a. The case $t > s_0\rho$

In this case the integration path is deformed to the vertical SDP through the origin, infinitesimally displaced on the right of the positive imaginary axis, as illustrated in Fig. 15. It can be noted that for $q < q_c$ the pole ω_{SPP} is captured and thus provides a residue contribution that will be denoted as $b''_{\phi SPP}(\rho,t)$:

$$b''_{\phi SPP}(\rho,t) = \mathrm{Re}\left\{\int_0^{q_c} (\omega_{SPP}s_0 - jq)H_1^{(2)}[(\omega_{SPP}s_0 - jq)\rho] \times \mathrm{Res}[D(q,\omega),\omega_{SPP}]\, e^{j\omega_{SPP}t}\, dq\right\}, \tag{B7}$$

where, of course, $\omega_{SPP} = \omega_{SPP}(q)$. Note that the upper integration limit has been set equal to q_c, since for $q > q_c$ the ω-SPP pole lies in the fourth quadrant and thus it is not captured in the path deformation.

On the other hand, for $q > q_d$ the pole $\omega_{p,3}$ lies in the first quadrant and thus it is also captured, and the relevant contribution will be denoted as $b_{\phi p3}(\rho,t)$:

$$b_{\phi p3}(\rho,t) = \mathrm{Re}\left\{\int_{q_d}^{\infty} (\omega_{p3}s_0 - jq)H_1^{(2)}[(\omega_{p3}s_0 - jq)\rho] \times \mathrm{Res}[D(q,\omega),\omega_{p3}]\, e^{j\omega_{p3}t}\, dq\right\}, \tag{B8}$$

where $\omega_{p3} = \omega_{p3}(q)$. Note that in this case the lower integration limit has been set to q_d, since for $q < q_d$ the pole $\omega_{p,3}$ lies on the imaginary axis and thus is not captured in the path deformation.

Note that the residues in (B7) and (B8) can be calculated analytically from (A7). The result is

$$\mathrm{Res}[D(q,\omega),\omega_p] = -\frac{j\mu_0}{2\pi} I(\omega_p)\ell(\omega_p s_0 - jq) \times \frac{\sqrt{2j\omega_p s_0 q + q^2}}{16s_0^2\bar{L}_g^2\omega_p^3 - 24js_0^2\bar{R}_g\bar{L}_g\omega_p^2 - 8s_0^2\bar{R}_g^2\omega_p + 2js_0 q}, \tag{B9}$$

where $\omega_p = \omega_{SPP},\omega_{p,3}$.

The considered source spectrum (21) has a pole in the first quadrant at $\omega_{ps} = \omega_0 + ja$ that is independent of q and is thus always captured in the path deformation. The relevant residue contribution is

$$b_{\phi ps}(\rho,t) = \mathrm{Re}\left\{\int_0^{\infty} (\omega_{ps}s_0 - jq)H_1^{(2)}[(\omega_{ps}s_0 - jq)\rho] \times \mathrm{Res}[D(q,\omega),\omega_{ps}]\, e^{j\omega_{ps}t}\, dq\right\}, \tag{B10}$$

where

$$\mathrm{Res}[D(q,\omega),\omega_{ps}] = -\frac{j\mu_0}{2\pi}\frac{I_0}{2}\ell \times \frac{(\omega_{ps}s_0 - jq)\sqrt{2j\omega_{ps}s_0 q + q^2}}{4\omega_{ps}^2 s_0^2 \bar{Z}_g^2(\omega_{ps}) - 2j\omega_{ps}s_0 q - q^2}. \tag{B11}$$

Finally, the ω-SDP integral gives rise to a fourth contribution, which will be denoted as $b_{\phi SDP^2}(\rho,t)$:

$$b_{\phi SDP^2}(\rho,t) = \mathrm{Re}\left\{\int_0^{\infty}\int_{q/(2s_0)}^{\infty} j\frac{(ps_0 - q)}{2\pi} H_1^{(2)}[j(ps_0 - q)\rho] \times D(q,\omega = jp)e^{-pt}\, dp\, dq\right\}. \tag{B12}$$

Here the integration along the ω-SDP has been parameterized by letting $\omega = jp$, $p \in \Re_0^+$ and the lower integration limit has ben set to $q/(2s_0)$, since for $p < q/(2s_0)$ the integrand is purely imaginary and hence gives no contribution to (B12).

Note that when $q < q_d$, the pair of poles $\omega_{p,i}$, $i = 3,4$ is located on the imaginary axis, i.e., $\omega_{p,i} = jp_{p,i}$, $i = 3,4$. An analysis of (B6) shows that $p_{p,i} > q/(2s_0)$, i.e., these poles always lie on the ω-SDP. However, the relevant residue contributions to the integral are purely imaginary; therefore they do not contribute to $b_{\phi SDP^2}(\rho,t)$, and thus the p integral can be evaluated as a Cauchy principal value around those poles or, alternatively, the ω-SDP can detour around them either on the left or on the right side.

Taking into account the four previously described contributions, we may write

$$b_{\phi SDP}(\rho,t) = b''_{\phi SPP}(\rho,t) + b_{\phi p3}(\rho,t) + b_{\phi ps}(\rho,t) + b_{\phi SDP^2}(\rho,t), \tag{B13}$$

so that from (5), (B1), and (B13), the *complete* TD field for $t > s_0\rho$ can finally be written as follows:

$$b_\phi(\rho,t) = b^{i}_\phi(\rho,t) + b'_{\phi SPP}(\rho,t) + b''_{\phi SPP}(\rho,t) + b_{\phi p3}(\rho,t) + b_{\phi ps}(\rho,t) + b_{\phi SDP^2}(\rho,t), \tag{B14}$$

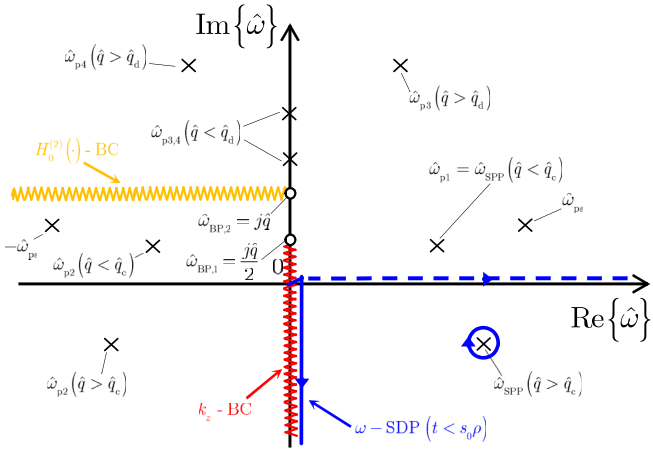

FIG. 16. Same as in Fig. 15, for $t < s_0\rho$.

i.e., as the sum of six contributions—the incident field b^{i}_{ϕ}, three graphene-related pole contributions $b'_{\phi\mathrm{SPP}}$, $b''_{\phi\mathrm{SPP}}(\rho,t)$, and $b_{\phi\mathrm{p3}}(\rho,t)$ (the first one arising from a k_ρ pole, the latter two from ω poles), one source-related pole contribution $b_{\phi\mathrm{ps}}$, and a double-integral SDP contribution $b_{\phi\mathrm{SDP}^2}$.

b. The case $t < s_0\rho$

In this case, the ω-SDP lies along the negative imaginary axis and thus the only pole singularity that can be involved in the process is ω_{SPP}, which is captured when $q > q_{\mathrm{c}}$ (see Fig. 16).

The complete TD field can thus be written as

$$b_\phi(\rho,t)=b^{\mathrm{i}}_{\phi}(\rho,t)+b'_{\phi\mathrm{SPP}}(\rho,t)+b''_{\phi\mathrm{SPP}}(\rho,t)+b_{\phi\mathrm{SDP}^2}(\rho,t), \tag{B15}$$

where

$$b''_{\phi\mathrm{SPP}}(\rho,t) = -\mathrm{Re}\left\{\int_{q_{\mathrm{c}}}^{+\infty}(\omega_{\mathrm{SPP}}s_0 - jq)H_1^{(2)}[(\omega_{\mathrm{SPP}}s_0 - jq)\rho]\right.$$
$$\left.\times\,\mathrm{Res}[D(q,\omega),\omega_{\mathrm{SPP}}]\,e^{j\omega_{\mathrm{SPP}}t}\,dq\right\} \tag{B16}$$

and

$$b_{\phi\mathrm{SDP}^2}(\rho,t) = \mathrm{Re}\left\{\int_0^{\infty}\int_0^{\infty} j\frac{(ps_0+q)}{2\pi}\,H_1^{(2)}[-j(ps_0+q)\rho]\right.$$
$$\left.\times D(q,\omega=-jp)e^{pt}\,dp\,dq\right\}. \tag{B17}$$

3. Causality

The total field is identically zero before the first wave-front arrival, i.e., for $t < s_0\rho$, as required by causality. In fact, let us consider the terms in (B15). The incident field b^{i}_{ϕ} is from (6) manifestly zero for $t < s_0\rho$. As concerns $b_{\phi\mathrm{SDP}^2}$, the integrand in (B17) is purely imaginary, so that also this term vanishes identically.

As concerns $b'_{\phi\mathrm{SPP}}$ and $b''_{\phi\mathrm{SPP}}$, these contributions are both different from zero; however, it can be shown that for $t < s_0\rho$, they are exactly equal and opposite [24]. In fact, by performing the change of variable $\omega = \omega_{\mathrm{SPP}}(q)$, the q integral in (B16) is transformed into an ω integral along the pole locus $\omega_{\mathrm{SPP}}(q)$, parameterized by $q \in [q_{\mathrm{c}}, +\infty)$, whose integrand is equal and opposite to the integrand in (B2). By deforming the integration path onto the real interval $[\omega_{\mathrm{c}}, +\infty)$, as is permissible thanks to the exponentially damped behavior at infinity of the integrand and the absence of captured singularities, we obtain (B2) with the sign changed and we may then conclude that $b'_{\phi\mathrm{SPP}} = -b''_{\phi\mathrm{SPP}}$, as claimed.

[1] F. H. L. Koppens, D. E. Chang, and F. J. García de Abajo, Nano Lett. **11**, 3370 (2011).
[2] K. G. Batrakov, V. A. Saroka, S. A. Maksimenko, and C. Thomsen, J. Nanophot. **6**, 061719 (2012).
[3] Y. V. Bludov, A. Ferreira, N. M. R. Peres, and M. I. Vasilevskiy, Int. J. Mod. Phys. B **27**, 1341001 (2013).
[4] F. J. Garcia de Abajo, ACS Photonics **1**, 135 (2014).
[5] A. Vakil and N. Engheta, Science **332**, 1291 (2011).
[6] A. Vakil and N. Engheta, Phys. Rev. B **85**, 075434 (2012).
[7] E. Forati and G. W. Hanson, J. Opt. **16**, 089501 (2014).
[8] E. H. Hwang and S. Das Sarma, Phys. Rev. B **75**, 205418 (2007).
[9] S. A. Mikhailov and K. Ziegler, Phys. Rev. Lett. **99**, 016803 (2007).
[10] G. W. Hanson, J. Appl. Phys. **103**, 064302 (2008).
[11] G. W. Hanson, J. Appl. Phys. **104**, 084314 (2008).
[12] G. Lovat, P. Burghignoli, and R. Araneo, IEEE Trans. Electromagn. Comp. **55**, 328 (2013).
[13] G. Lovat, R. Araneo, P. Burghignoli, and G. W. Hanson, IEEE Trans. THz Sci. Technol. **5**, 941 (2015).
[14] G. W. Hanson, A. B. Yakovlev, and A. Mafi, J. Appl. Phys. **110**, 114305 (2011).
[15] A. Y. Nikitin, F. Guinea, F. J. García-Vidal, and L. Martín-Moreno, Phys. Rev. B **84**, 195446 (2011).
[16] G. W. Hanson, E. Forati, W. Linz, and A. B. Yakovlev, Phys. Rev. B **86**, 235440 (2012).
[17] D. Margetis and M. Luskin, J. Math. Phys. **57**, 042903 (2016).
[18] M. Maier, D. Margetis, and M. Luskin, J. Comp. Phys. **339**, 126 (2017).
[19] S. A. Mikhailov, Europhys. Lett. **79**, 27002 (2007).
[20] A. Agrawal, H. Cao, and A. Nahata, New J. Phys. **7**, 249 (2005).
[21] L. B. Felsen, *Transient Electromagnetic Fields* (Springer-Verlag, Berlin, 1977).
[22] G. Lovat and R. Araneo, IEEE Trans. Nanotechnol. **14**, 681 (2015).
[23] G. Lovat, P. Burghignoli, R. Araneo, and S. Celozzi, IEEE Trans. Nanotech. (2018), doi:10.1109/TNANO.2018.2844872.
[24] L. Tsang and J. A. Kong, J. Math. Phys. **20**, 1170 (1979).
[25] A. Ezzeddine, J. A. Kong, and L. Tsang, J. Appl. Phys. **53**, 813 (1982).
[26] S. Y. Poh and J. A. Kong, J. Electromagn. Waves Appl. **1**, 153 (1987).

[27] J. Van Bladel, *Electromagnetic Fields* (Wiley - IEEE Press, Hoboken, NJ, 2007).
[28] L. A. Falkovsky, Physics-Uspekhi **51**, 887 (2008).
[29] G. Lovat, G. Hanson, R. Araneo, and P. Burghignoli, in *Proceedings of European Conference on Antennas and Propagation (EUCAP) 2013* (Gothenburg, Sweden, 2013), pp. 500–504.
[30] G. Lovat, G. W. Hanson, R. Araneo, and P. Burghignoli, Phys. Rev. B **87**, 115429 (2013).
[31] G. W. Hanson, IEEE Trans. Antennas Propag. **56**, 747 (2008).
[32] V. P. Gusynin, S. G. Sharapov, and J. P. Carbotte, J. Phys.: Condens. Matter **19**, 026222 (2007).
[33] G. Franceschetti and C. Papas, IEEE Trans. Antennas Propag. **22**, 651 (1974).
[34] W. C. Chew, *Waves and Fields in Inhomogenous Media* (IEEE Press, Piscataway, NJ, 1999).
[35] M. Abramowitz and I. A. Stegun, *Handbook of Mathematical Functions* (Dover, New York, 1965).
[36] R. E. A. C. Paley and N. Wiener, *Fourier Transforms in the Complex Domain* (American Mathematical Society, Providence, RI, 1934).
[37] F. Niu and L. B. Felsen, IEEE Trans. Antennas Propag. **41**, 755 (1993).
[38] CST MICROWAVE STUDIO, https://www.cst.com/products/cstmws, accessed: 2018-02-12.
[39] Quartic function, https://en.wikipedia.org/wiki/Quartic_function, accessed: 2018-02-12.